Materials Science & Engineering A 781 (2020) 139204

Contents lists available at ScienceDirect

Materials Science & Engineering A

journal homepage: www.elsevier.com/locate/msea

Microstructure evolution during indentation of Inconel-718 created by additive manufacturing

Mustafa Rifat, Edward C. DeMeter, Saurabh Basu *

Harold and Inge Marcus Department of Industrial and Manufacturing Engineering, Penn State University, University Park, PA, USA

ARTICLE INFO

Keywords:
Indentation
Surface roughness
Microstructure
Additive manufacturing

ABSTRACT

Finishing of components originating from additive manufacturing (AM) is critically important for providing them with adequate tolerances and fatigue life. These processes often rely on surface deformation for removal of roughness features and enhancing the underlying microstructures. Optimization of finishing processes is however challenging for AM components as their mechanics of deformation is complicated by microstructure/defect/roughness combinations present in as-received surfaces. In this work, the mechanics of surface deformation in additively manufactured IN718 is studied via indentation. Effects of graded surface microstructure, surface texture and porosity defects on microstructure evolution trajectories are delineated. Using these insights, a finite element based numerical framework of surface deformation of additively manufactured IN718 is created. Utility of this framework in analysis of surface deformation of various microstructure/defect/roughness combinations is demonstrated. Implications of these insights in the optimization of finishing processes of various additively created parts is discussed.

1. Introduction

Currently there is strong interest in using additive manufacturing (AM) processes to originate metallic parts for high performance applications. Additive manufacturing involves layer-by-layer deposition of material, wherein individual layers are consolidated with their substrate in a process that involves rapid melting and solidification using a localized heat source. This process is repeated until the specified geometry is completely built. Unfortunately as-printed surfaces originating from AM are rough and incapable of functioning as mating surfaces in a product assembly. Additionally, notch-like surface roughness features can act as sites of fatigue induced damage [1]. Hence, the surfaces of AM parts are typically subject to primary machining processes, peening processes, or secondary machining processes that use loose abrasives. These processes are used to create surfaces with tighter geometric control, reduced roughness, or residual compressive stresses.

The aforementioned finishing processes induce subsurface deformation, the mechanics of which is complicated by a multitude of parameters involving the underlying microstructure [2–4] and characteristics of the surface roughness [5]. Herein, AM can naturally produce a high density of volumetric-porosity defects [6,7] and unique microstructure characteristics [8–12], e.g. preferred crystallographic textures [13], and, gradients in grain size. The surface roughness of printed metal parts is also extremely sensitive to orientation relative to the build direction [14]. Down skin surfaces, subject to a combination of solidification roughness, staircasing, and partially solidified powder, can have roughness values 20 X larger than horizontal up-skin surfaces only subject to solidification roughness. Consequently, when subjected to finishing processes, the resulting subsurface microstructures could vary considerably depending on surface orientation. This will also influence subsurface microstructure and result in anisotropic performance metrics, which is of great concern for high performance applications.

Understanding how starting surface texture and subsurface microstructure may influence their evolution during finishing is important with regard to finishing process selection and design. In this regard, components originating from AM present novel challenges in finishing that have not been addressed. For instance, the directionality of the mechanics of finishing resulting from anisotropy in as received microstructures and surface textures necessitates optimization of the finish process parameters for achieving the desired surface state. Herein, a single set of process parameters is not expected to function equally effectively even over the different faces of a single component [1,15]. Addressing this knowledge gap requires an in-depth understanding of the mechanics of finishing in surface-texture/microstructure/defect combinations that originate from AM.

In this study, circular indentation is performed on Inconel 718 microstructure created by selective laser melting with the overarching goal of understanding the mechanism of microstructure evolution in

* Corresponding author.
E-mail address: sxb514@psu.com (S. Basu).

https://doi.org/10.1016/j.msea.2020.139204
Received 29 August 2019; Received in revised form 23 January 2020; Accepted 5 March 2020
Available online 10 March 2020

additively manufactured specimens during surface deformation. Attempt is made to delineate effects arising from surface roughness, microstructure gradients, and porosity defects. These insights are subsequently used to create a framework whose utility in optimizing finishing processes are discussed.

2. Experimental and computational

Inconel 718 specimens were printed in an EOS M280 direct metal laser sintering machine using EOS-718 powder. Power level was preset at 285 W with a laser spot diameter of 87.5 μm. The layer thickness was 40 μm. The completed build was vacuum stress relieved at $1065° \pm 12\,°C$ for 90 ± 15 min per EOS recommendations. Finally, the test piece was removed from the build plate using electric discharge machining. The test piece in this state will be referred to as pre-deformed for rest of the document.

Plane strain indentation was performed on the test piece using an alloy steel indenter featuring diameter $d = 5$ mm. A nominally smooth dowel pin purchased from McMaster Carr featuring a minimum Rockwell hardness C52 was used as the indenter. The orientation of the indenter with respect to the build direction is shown in Fig. 1a. Indentation was performed in the as-received condition described in the previous paragraph. The speed of indentation was 1 mm/min and the maximum depth was $h_{max} \sim 0.09$ mm. The displacement field in the indentation specimen was recorded in a sequence of images using a PCO.edge high speed camera that was equipped with an infinity microscopic lens. The lens assembly in the current setup provided a resolution of 15 μm/pixel. A bright light source was used to illuminate the scanned face while imaging. Fig. 1b shows an image in this sequence. The displacement field was subsequently characterized using digital image correlation. This involved finding the zero normalized correlation coefficient: $\Phi_k(m,n) = \Sigma_{j=1}^{q} \Sigma_{i=1}^{p} f_k(i,j) f_{k+1}(i+m, j+n)$, where $f_k(i,j)$ is intensity of pixel (i,j) in image k that is zero normalized. Zero normalization refers to subtracting mean of all pixel values and dividing the result with standard deviation. By locating the maxima in the parameter $\Phi_k(m,n)$, displacement vector $(u_x, u_y) = (m,n)$ incurred by the material point at pixel (i,j) in image k is found. By doing this repeatedly over all pixels in the region of interest, the displacement field is characterized. Calibration of the method by characterization of Young's moduli of known materials showed that strains as small as 10^{-4} could be reliably measured using this method. The characterized displacement field was subsequently differentiated spatially with respect to the original grid to find the deformation tensor at the end of deformation as $\mathbf{F} = \nabla u + \mathbf{I}$, from which the Left Green–Lagrange strain tensor was extracted as $\mathbf{E} = 1/2(\mathbf{F}^T\mathbf{F} - \mathbf{I})$. Microstructure characterization by Orientation Imaging Microscopy (OIM) was performed using a FEI Helios 660 SEM equipped with Oxford HKL electron back scattered diffraction detector. Characterizations were performed at 20 KV and 6.4 nA. A zone ~130 μm thick directly underneath the surface was scanned with a step size of 0.55 μm. This was done in pre and post deformed conditions. AZtec software provided by Oxford Instruments was used to extract raw data, which was subsequently processed using the open source Matlab library called MTEX 5.1.1. Using this Matlab library, various microstructure statistics were extracted as described in the forthcoming sections.

Experimental strain mapping and microstructure characterization were supplemented with implicit finite element simulations of plane strain indentation using Abaqus. For the same, the indenter was treated as a rigid body. The bulk workpiece was treated as an isothermal Johnson–Cook material featuring constants (A, B, n, m, Tm) = (450 MPa, 1.7 GPa, 0.65, 1.3, 1609 K) [16]. Assigned density, elastic modulus and Poisson's ratio of the workpiece were 9000 Kg/m^3, 200 GPa, and 0.29, respectively. Elements of type CPE4R featuring plane strain thickness 0.008 mm were assigned to both indenter and workpiece. Friction coefficient $\mu_f = 0.64$ was used corresponding to steel-Ni interfaces. This value for friction coefficient was validated by investigating several friction coefficients, viz. $\mu_f = 0.1, 0.5, 0.64, 0.99$, and sticking, wherein it was seen that $\mu_f = 0.64$ resulted in reasonable prediction of process mechanics. For delineating the effect of surface roughness on indentation, representative surface-profiles were obtained from the as-received specimen using secondary electron imaging. These profiles were then imported into the simulated workpiece using the python scripting interface of Abaqus.

3. Results

3.1. Deformation mapping

Results of displacement and strain mapping are shown in Fig. 2. Figs. 2a–2c show horizontal (u_x mm), vertical (u_y mm) components, and magnitude ($\sqrt{u_x^2 + u_y^2}$ mm) of displacement field, respectively. Fig. 2c shows that the displacement field at $(r,\theta) = (0\ \mu m, 0°)$ exhibits a maximum value ~0.09 mm. This value decayed progressively at larger distances r with respect to surface of the indenter. The displacement field was differentiated spatially and processed to find the Left Green–Lagrange strain E. Horizontal, vertical and shear components, i.e. E_{11}, E_{22}, E_{12}, respectively, are shown in Figs. 2d–2f. These fields were calculated within the zone marked in the white rectangle in Fig. 1b. Local maxima in absolute values of strains were seen at zones located in the vicinity of the free surface of the workpiece close to $(r,\theta) = (0\ \mu m, 8.9°)$, pointed using white arrows in Figs. 2d–2f. These were, $(E_{11}, E_{22}, E_{12}) = (0.04, -0.16, -0.25)$, and $(-0.05, 0.1, 0.17)$ for $(r,\theta) = (0\ \mu m, -8.9°)$ and $(r,\theta) = (0\ \mu m, 8.9°)$, respectively. Directly underneath the indenter, i.e. $(r, 0°)$ for $r > 0$, a dead metal zone was observed exhibiting negligible strains in both positive and negative sense, i.e. $(|E_{11}|, |E_{22}|, |E_{12}|) \to (0,0,0)$.

The strain fields shown in Figs. 2d–2f exhibit several local spikes in addition to the local maxima/minima near $(r,\theta) = (0\ \mu m, 8.9°)$. These spikes exhibit waviness, i.e. oscillation between high positive and negative values. Further, these spikes exhibit periodicity, an instance of which is pointed using black arrow in Figs. 2d, 2e. In order to delineate these characteristics, a waterfall plot was generated using Fourier analysis of the E12 strain component field (Fig. 2f), as shown in Fig. 3. This plot suggests that spikes in the strain field near the free surface of the test specimen could exhibit wavelengths as small as $\lambda > 0.2$ mm. Prominent wave components featuring wavelengths of this order are pointed using black arrows in Fig. 3. The wavy nature of the strain field featuring low wavelengths of the same order, e.g. $\lambda < 1$ mm, decayed at larger depths with respect to the indented surface as indicated by absence of similar spikes there, in the waterfall plot. While this absence is partly due to a general decay of strain with respect to increasing depths, it can also be due to a concomitant subjugation of the physical phenomena, which originally caused waviness in the strain field near the free surface. The dominant presence of large wavelength components at larger depths with simultaneous absence of low wavelength component in Fig. 3 partially corroborates this hypothesis. Possible reasons behind these phenomena are discussed in the forthcoming sections. Note for reference, optical characterization equipment used for this research enables resolution, i.e. sampling at 0.014 mm/pixel, this being $< 0.5\lambda$ (<0.1 mm) required to reliably detect anomalies occurring over wavelengths $> \lambda$(>0.2 mm) as prescribed by the Nyquist criterion.

3.2. Orientation imaging microscopy

3.2.1. Pre-deformed microstructures

Fig. 4 shows results of microstructure characterization on cross sections of the workpiece in the pre-deformed state. Fig. 4a shows the orientation imaging micrograph of grains in the cross section normal to the build direction Z shown in Fig. 1. In this state, the microstructure exhibited gradients in grain size as quantified in Fig. 4b. A zone comprising grains in immediate vicinity of the free surface $r = 0$ μm

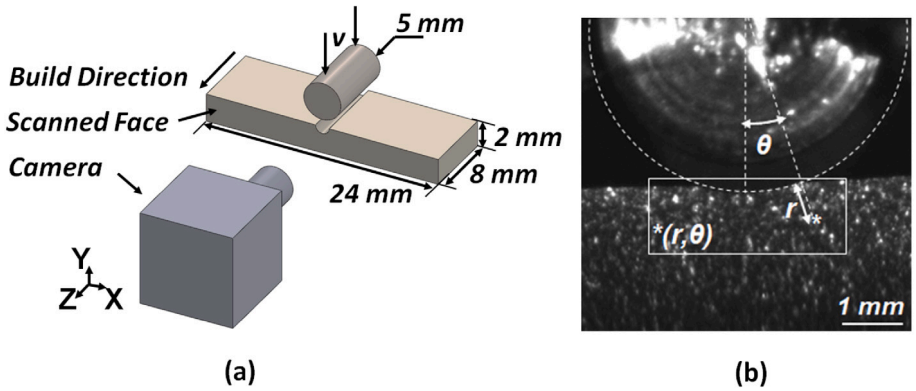

Fig. 1. (a) Orientation of indentation with respect to build direction, (b) Optical characterization of indentation and reference axis.

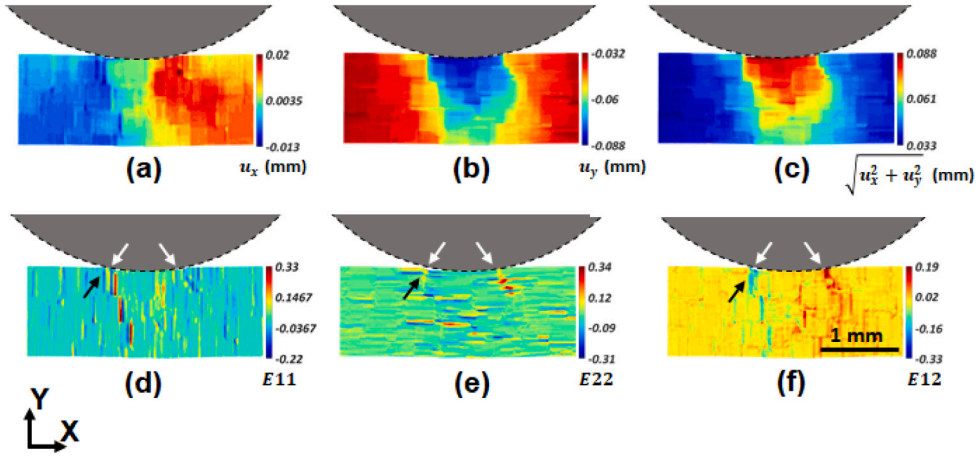

Fig. 2. Displacement field showing components: (a) u_x, (b) u_y, and (c) magnitude. Left Cauchy-Lagrangian strain components are shown in (d) E_{11}, (e) E_{22}, and (f) E_{12}.

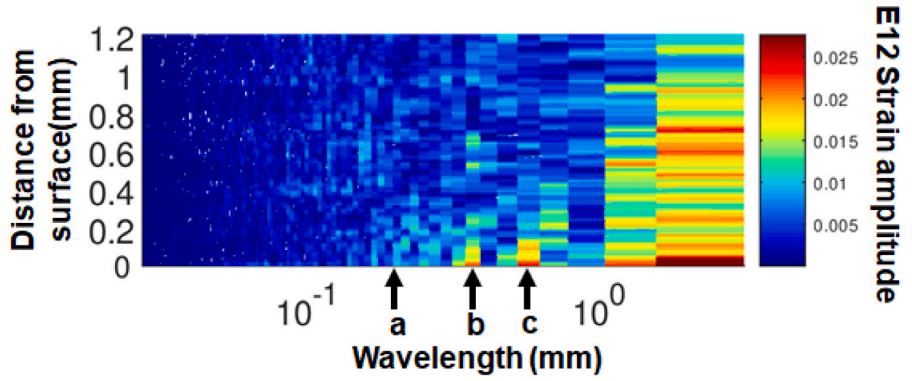

Fig. 3. Waterfall plot of strain field E_{12} shown in Fig. 2f. The arrows correspond to wavelengths: (a) $\lambda = 0.21$ mm, (b) $\lambda = 0.4$ mm, (c) $\lambda = 0.63$ mm.

exhibited twins that were 1 μm–10 μm wide, with parent grains featuring diameters ~ 30 μm. Fig. 4c shows the Grain Orientation Spread (*GOS*) extracted from the pre-deformed microstructure. The parameter *GOS* is given by $GOS = \frac{1}{N(N-1)} \Sigma_{i=1}^{N} \Sigma_{j=1}^{N} \Delta g(g_i, g_j)$ and refers to the average misorientation between all points in a grain. Here, a grain is defined as a zone enclosed by a boundary featuring disorientation >15°. Parameters g_i, g_j, N refer to orientation at point i,j, respectively, in a grain that contains N points characterized by OIM. The *GOS* field exhibits spread in the pre-deformed microstructure, featuring values between 0°–15°, with an area weighted mean of 3.48°.

The mean GOS of a polycrystalline microstructure increases during imposition of strains due to formation of dislocation structures in constituent grains [17,18]. These dislocation structures subdivide a grain into several off-spring sub-grains, each disoriented with respect to its neighbor. Imposition of sufficient strains results in the disorientation between neighboring sub-grains to cross over into high angle (>15°) regimes. In this manner, a grain fragments into several off-spring grains during imposition of strains, and this process is known as Continuous Dynamic Recrystallization (CDRX). Each grain resulting from this subdivision process continues to undergo refinement in a similar manner with imposition of further strains and the process repeats. Investigations have identified a threshold GOS=2.6° to distinguish between freshly recrystallized, i.e. $GOS < 2.6°$ and deformed, i.e. $GOS > 2.6°$ grains [17]. In this regard, our AM workpiece exhibits a low-moderate $GOS = 3.48°$, reminiscent of the thermal history imposed during AM + heat treatment steps.

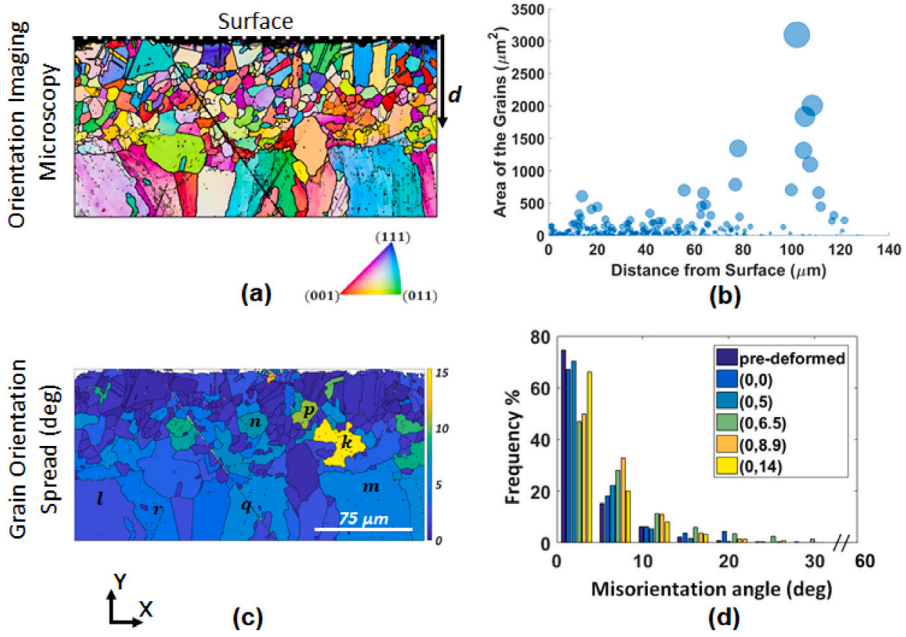

Fig. 4. Microstructure in the pre-deformed material. (a) Orientation Imaging Microscopy, (b) Variation in grain size with respect to distance d from the surface, (c) Grain Orientation Spread, (d) Misorientation angle distribution in microstructures at specified zones. Thick and thin black lines correspond to boundaries featuring disorientation 15° and 1°, respectively.

Fig. 4d shows the misorientation distribution of the microstructure created by AM, in the pre-deformed state. The distribution shows that a high fraction ~ 75% of neighboring points exhibited low <3° disorientation. This fraction decayed monotonically with ~3.7% of neighboring points exhibiting disorientations > 15°. These characteristics of misorientation distribution were reflected in the microstructure, where most grains featured negligible (0.1°/μm–0.5°/μm) intra-grain misorientation gradients along randomly oriented directions. Grains that featured large areas, labeled l,m,q,r in Fig. 4b, and those featuring high *GOS*, i.e. n, p, q exhibited higher densities of low angle 1° grain boundaries in comparison with other grains. Low 1° and high 15° boundaries are demarcated using thin and thick white lines in Fig. 4a, respectively.

3.2.2. Deformed microstructures

Figs. 5a–5e show microstructures resulting from indentation with their corresponding GOS fields in Figs. 5f–5j, respectively. These microstructures were obtained from zones in vicinity of the free surface between depths r = 0 μm–130 μm. Their center points approximately corresponded to locations $(r,\theta) = (65\ \mu m, 0°), (65\ \mu m, 5°), (65\ \mu m, 6.5°), (65\ \mu m, 8.9°)$, and $(65\ \mu m, 14°)$, respectively. Absolute values of empirically characterized strain tensor components at these locations were $(|E_{11}|, |E_{22}|, |E_{12}|) = (0, 0.07, 0.01), (0.02, 0.08, 0.05), (0.06, 0.12, 0.05), (0.15, 0.1, 0.17), (0, 0.19, 0.02)$, respectively. Qualitatively, these microstructures exhibited similar gradients in grain size and grain shapes as their pre-deformed counterpart. This is expected given moderate amounts of deformation imposed in our indentation experiment that would only cause moderate changes to these metrics. However, area weighted GOS parameters extracted from these microstructures exhibited considerable differences with respect to the pre-deformed material with GOS=4.79°, 3.85°, 7.01°, 5.77°, 4.5°, respectively.

Fig. 4d shows the misorientation distribution extracted from these microstructures, overlaid on top of that obtained from the pre-deformed material. Microstructures directly underneath the indenter and slightly to the side, i.e. $(r,\theta) = (0\ \mu m, 0°), (0\ \mu m, 5°)$, respectively, exhibited characteristics that were similar to the pre-deformed state. These characteristics included high fractions of neighboring points featuring low disorientations < 3°, at 67%, and 70%, respectively. However, there was a slight increase in point-pairs that exhibited disorientations > 15° in microstructures directly underneath the indenter $(r,\theta) = (0, 0°)$, at 8.5%. At larger angles with respect to the central axis, $(r,\theta) = (0, 6.5°)$ and $(0, 8.9°)$, microstructures exhibited considerable differences with respect to the pre-deformed material. These differences include a drop in fraction of neighboring points that featured a disorientation < 3°, e.g. from ~75% to 57%, and 50%, respectively. Simultaneously, neighboring points at these locations that featured a disorientation > 15° rose from 3.7% to 13.44%, and 6.11%, respectively. Characteristics of microstructure at location $(r,\theta) = (0\ \mu m, 14°)$ reverted back to those seen in the material in the pre-deformed state, e.g. a high, 66% of neighboring points featuring disorientation < 3°, and 5.6% neighboring points showing disorientation > 15°. Characteristics of misorientation distribution were seen in the grain boundary structure in Figs. 5c and 5d. Grains in these zones that featured high area or orientation spreads also exhibited high densities of low angle 1° grain boundaries. In comparison with material in the pre-deformed state, these grains in the deformed material exhibited significantly larger densities of such low angle boundaries. Microstructures obtained from the indented specimen also exhibited highly concentrated deformation between zones bridging porosity defects. This is illustrated in the dashed white box in Fig. 5d corresponding to zone $(r,\theta) = (0\ \mu m, 8.9°)$. Here, two porosity like features are seen to be surrounded by grains featuring high *GOS* ~ 11°.

3.3. Effect of microstructure gradients on material response during indentation

Microstructures obtained from the deformed specimen exhibit features that are commonly seen during progressing continuous dynamic recrystallization (CDRX). For instance, locations $(r,\theta) = (0\ \mu m, 8.9°), (0\ \mu m, 6.5°)$ lie in vicinity of the zone that exhibits local maxima in strain and microstructures obtained from these zones exhibit the highest fraction of point pairs that feature larger disorientations as seen in Fig. 4d. Similarly, these locations also exhibit largest area weighted GOS parameters. None the less, these microstructures exhibit heterogeneity in deformation, as evidenced from the GOS fields (Figs. 5f–5j) that exhibit highly separated global maxima and minima. In order to delineate this phenomenon, the GOS parameter was

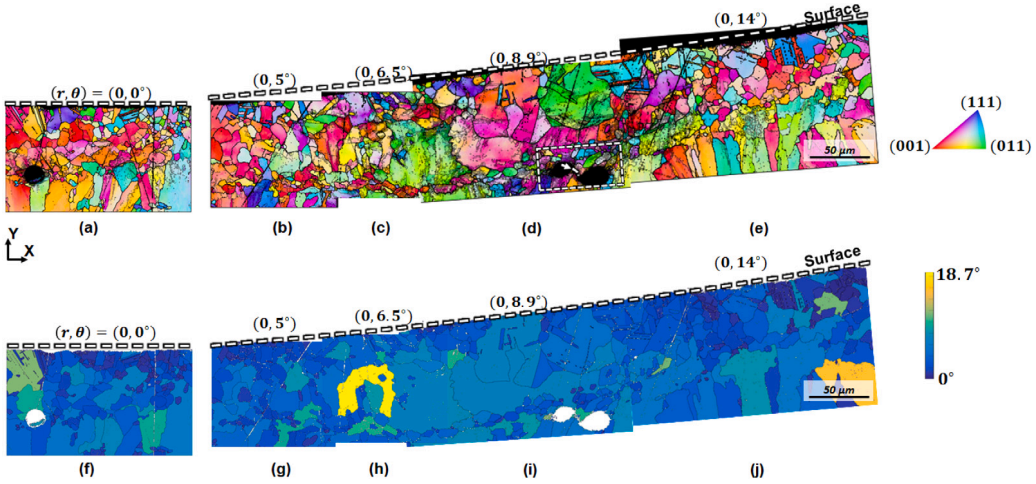

Fig. 5. (a–e) Orientation imaging microscopy and (f–j) grain orientation spread of microstructures resulting from indentation.

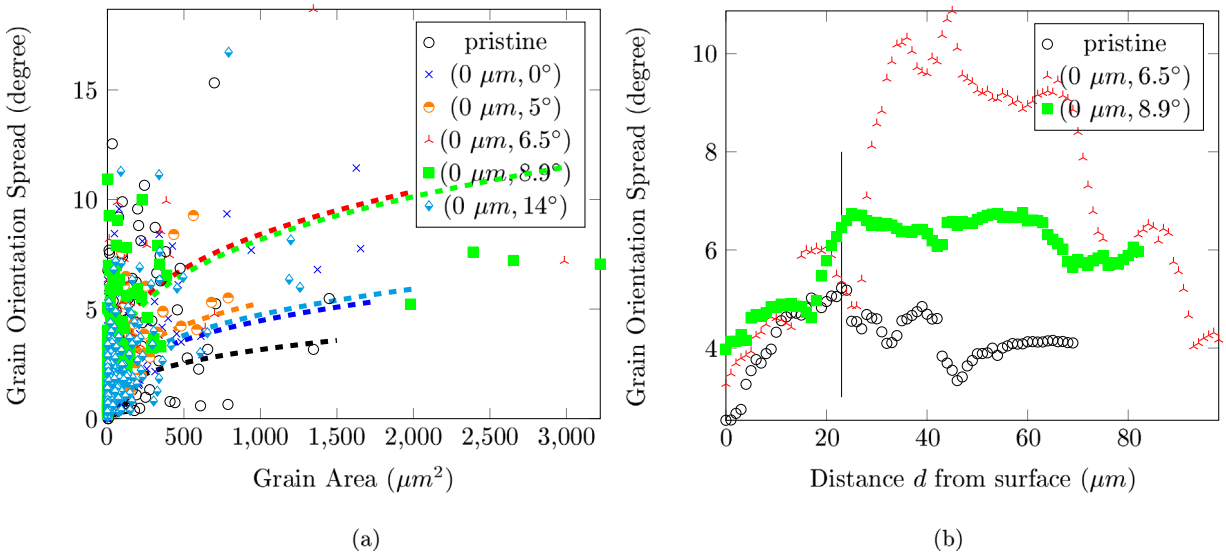

Fig. 6. Characteristics of deformed grains resulting from indentation.

plotted with respect to grain area A and is shown in Fig. 6a. Area was chosen as the x-axis for these iso-strain plots due to known inverse effect of grain-size on strain hardening [19–21]. Considerable scatter was seen in the obtained plots indicating the heterogeneity in deformation. In order to delineate the scatter in the data, power law curves were fitted to the obtained GOS vs. Grain area profiles in pre-deformed microstructure as well as those in $(r, \theta) = (0\ \mu m, 0°), (0\ \mu m, 5°), (0\ \mu m, 6.5°), (0\ \mu m, 8.9°)$, and $(0\ \mu m, 14°)$. These were found to be $GOS = 0.37A^{0.31}, 0.49A^{0.32}, 0.62A^{0.31}, 1.059A^{0.3}, 0.96A^{0.31}, 0.52A^{0.32}$, these equations exhibiting goodness of fits $R^2 = 0.2, 0.2, 0.59, 0.52, 0.53, 0.41$, respectively. A lower goodness of fit indicates poorer choice of independent-variable/model for modeling data. This was the case for the pre-deformed microstructure and that found directly underneath the indenter in the dead metal zone i.e. $(r, \theta) = (0\ \mu m, 0°)$, both exhibiting $R^2 = 0.2$. However with incremental deformation, a larger dependence on area was seen with microstructures at $(r, \theta) = (0\ \mu m, 5°), (0\ \mu m, 6.5°), (0\ \mu m, 8.9°)$ exhibiting $R^2 = 0.59, 0.52, 0.53$. This dependence reduced to $R^2 = 0.41$ at location $(r, \theta) = (0\ \mu m, 14°)$, which also showed a reversal in its microstructure characteristics, e.g. misorientation distribution, to near pre-deformed levels.

The aforementioned grain-area dependence suggests that microstructure in the vicinity of the surface ($r < 30\ \mu m$), which is mostly occupied by small grains does not effectively accommodate deformation imposed during indentation. Evidence for this behavior was found in GOS plots shown in Fig. 5h and 5i that feature a high concentration of grains in vicinity of the surface that exhibit low orientation spreads despite exhibiting higher GOS in grains at larger depths. This trend was also captured in GOS vs. depth from surface profiles for microstructures obtained from the pre-deformed specimen and that in locations $(r, \theta) = (65\ \mu m, 6.5°), (65\ \mu m, 8.9°)$. The trend is shown in Fig. 6b and exhibits almost no difference in zones characterized by $r < 23\ \mu m$ demarcated using vertical black line.

4. Discussion

The aforementioned results indicated heterogeneity in deformation during indentation of additively manufactured IN718. Plausible sources of this heterogeneity can be hypothesized as: interaction of surface roughness features with the indenter, harder microstructure zones close to the surface in AM specimens, and porosity defects. In order to assess the contributions of these effects, a numerical model of indentation is created here as shown in Fig. 9a. To capture effects of roughness features within the numerical model, a representative pre-deformed surface profile was characterized from secondary electron imaging of the polished cross section normal to the build direction. This profile was then quantified using Matlab and used as input while creating

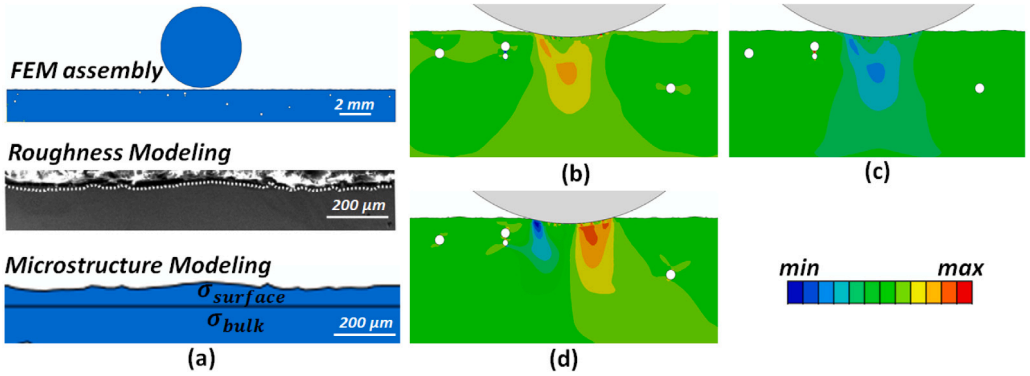

Fig. 7. (a) Finite Element Method (FEM) assembly of indentation showing roughness modeling and microstructure modeling, and strain fields (b) E_{11} (c) E_{22}, and (d) E_{12}. The inset on the bottom right shows the colorbar. Maximum and minimum values of the strain fields are $min, max\ E_{11} = -0.23, +0.16$, $min, max\ E_{22} = -0.26, +0.19, min, max\ E_{12} = -0.26, +0.19$.

surface of the simulated workpiece. The middle inset in Fig. 7a shows the representative profile, featuring length $\sim$ 1.3 mm, R_a = 6.5 μm and maximum height between peak and valley $maxR_t \sim 30$ μm. The roughness peaks featured widths between 20 μm–400 μm. The profile was repeated over the entire surface of the simulated plane-strain specimen that was subject to indentation. Friction coefficient $\mu_f = 0.64$ was used, and indentation was simulated using conditions analogous to real experiments. The indented workpiece was also endowed with a harder zone close to the surface to model the phenomena that results from graded microstructures seen in our IN718 specimen. This gradation is illustrated in Fig. 4b and suggests a grain size of ~10 μm at depths $d < 80$ μm and a grain size $\sim$ 50 μm in the bulk. Herein, an approach analogous to [22,23] was used wherein the surface layer up to a depth $d < 80$ μm was assigned a flow stress $\sigma_{surface} = 1.7\sigma_{bulk}$. Analogous behavior was seen in pure Ni [24] wherein reduction in grain sizes from ~50 μm to ~10 μm resulted in a 1.7× increase in the yield strength. The bulk flow stress refers to Johnson–Cook flow behavior whose parameters are given in Section 2. Finally, the effect of circular porosity on surface deformation was analyzed by implanting such defects in the numerically simulated specimen. This was done by sampling circular porosity defects with uniformly distributed diameters ranging between 30 μm–60 μm. A low density (0.25 defects/mm^2) of defects were distributed in random locations in the specimen. This arrangement and density of defects was motivated from our post-deformed specimen shown in Fig. 5.

4.1. Understanding the response of AM fabricated IN718 specimens

Isotropic material simulations summarized in Fig. 7 generally show that presence of roughness on surface can result in asymmetry in mechanics of indentation about its central axis, i.e. $(r > 0, 0°)$. This asymmetry is most evident in shear components $PE12$ that exhibit global maxima and minima of $PE12 = +0.19, -0.26$, respectively. Further, Fig. 7 also shows that roughness results in considerable heterogeneity in strain during indentation with several localized zones near the surface exhibiting spikes in strain tensor components as also seen in empirical characterization by DIC. In addition to factors resulting from roughness, strain field spikes were also seen in the vicinity of porosity defects that exhibited deviations between positive and negative values.

The effect of the harder near-surface microstructure zone on mechanics of indentation can be assessed from Fig. 8a that illustrates the effective strain field in the specimen. It was seen from this field that the harder microstructure zone is ineffective at accommodating high strains during indentation, wherein deformation imposed by the indenter is dominantly accommodated by the softer bulk. This numerically simulated result reflects empirical observations summarized in Section 3.3 and Fig. 6, where it was shown that the microstructure zone close to the surface exhibited smaller average grain orientation spread suggesting delayed progression through stages of continuous recrystallization.

4.2. Formulating finish routines for additively manufactured components

Validation of the numerical framework of indentation for predicting mechanics of surface deformation as shown in Section 4.1 allows its use in formulating finish routines for additively manufactured parts. Such frameworks can enable optimization of finish process parameters without necessitating trial-error runs by facilitating accurate predictions of surface deformation across different combinations of as-received surface textures and microstructures. The following subsections demonstrate this utility.

4.2.1. Effect of thicker surface graded zone

The effect of a thicker graded zone near the surface that features higher hardness than the bulk was assessed by simulating the mechanics of indentation under equivalent conditions. Herein, the thickness of the graded zone was increased 5× by assigning the material within the zone $d < 400$ μm a flow stress $\sigma_{surface} = 1.7\sigma_{bulk}$. Analogous conditions, e.g. a thick graded zone can arise in additive manufacturing as a consequence of spatial variations in elemental compositions [25], intermediate plastic deformation, e.g. hybrid manufacturing [26], or directly from the spatially tuned dynamics of heat [27]. The same surface texture and porosity defect structure as Fig. 7 was used and indentation was simulated up to the same depth $h_{max} = 90$ μm. Fig. 8b shows the effective strain field resulting from indentation in this surface texture/microstructure combination. Compared to the scenario involving a thinner graded microstructure zone, the strain field here exhibited a more diffuse character with deformation percolating to larger depths. This suggests that scenarios involving a thicker hardened surface zone present a greater challenge from the context of surface finishing as the strain imposed naturally tends to spread out to larger depths, thereby not contributing to deformation induced removal of surface roughness features. An analogous characteristic was reported in [28] where shot peening was shown to produce a smoother surface due to less material removed via deformation if the surface had been hardened by nitriding prior to the peening treatment.

4.2.2. Effect of micro-meter scale surface roughness

In order to assess the effect of micro-meter scale surface roughness, finite element analysis of indentation on workpiece featuring simple sinusoidal roughness was performed. The sine wave used was $y = A\sin(\frac{2\pi}{\lambda})$, with amplitude A being $A = 20$ μm, 40 μm, and wavelength λ being $\lambda = 240$ μm, 480 μm. Effects arising from porosity defects and graded microstructures were disregarded in these simulations. Fig. 9 shows snapshots of these simulations that were obtained at the same indentation depth 90 μm with respect to the first contact between the indenter and the surface. At the same depth, the simulated specimens exhibited mechanics that were different from each other. Parameters extracted here illustrate these differences and suggest that their origins were rooted in the surface roughness features

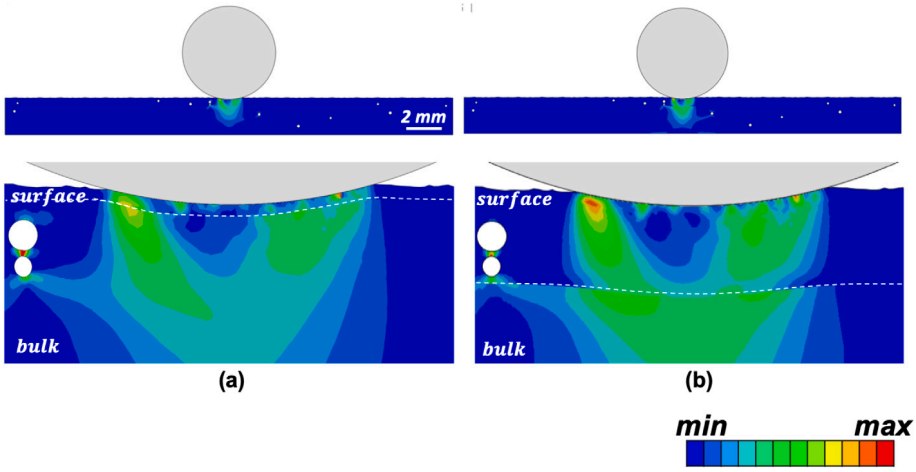

Fig. 8. Effect of graded microstructure on mechanics of indentation illustrated via their effective strain fields. The graded zones features a flow stress $\sigma_{surface} = 1.7\sigma_{bulk}$ up to depths of (a) $d < 80$ μ (also elaborated in Fig. 7), (b) $d < 400$ μm. The inset on the bottom rights shows the color bar with respect to which, the minimum,maximum values for the strain fields correspond to 0,0.27 and 0,0.21 for (a) and (b), respectively.

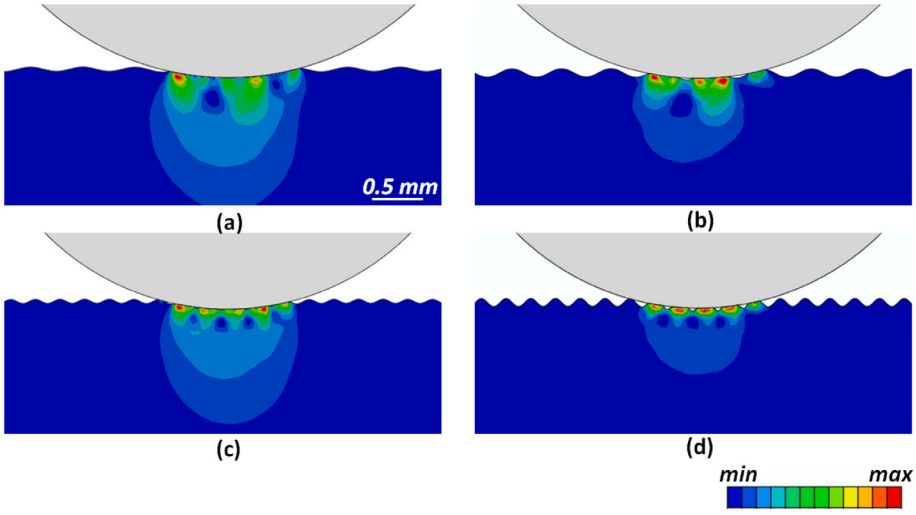

Fig. 9. Effective strain fields generated during indentation of surfaces with sinusoidal roughness features characterized as $y = A\sin\frac{2\pi}{\lambda}$, with wave parameters (A, λ) being: (a) (20 μm, 480 μm), (b) (40 μm, 480 μm), (c) (20 μm, 240 μm), (d) (40 μm, 240 μm). Coefficient of friction $\mu_f = 0.64$ was used for these simulations. The minimum value is 0 in all strain fields. The maximum value for the respective strain fields is ϵ = (a) 0.31, (b) 0.38, (c) 0.35, (d) 0.54.

themselves. For instance, the maximum effective strain imposed during indentation increased with respect to increase in amplitude A and decreased with increase in wavelength λ. These were found to be $\epsilon = 0.31, 0.38, 0.35, 0.54$ for waves featuring parameters $(A, \lambda) =$ (20 μm, 480 μm), (40 μm, 480 μm), (20 μm, 240 μm), (40 μm, 240 μm), respectively. Strain fields obtained from these simulations also exhibited periodic variations close to the indented surface at the same frequency as the sinusoidal roughness profile. Fig. 9 suggests that deformation is localized near the surface of the specimen when size of the indenter is large compared to the amplitude of the roughness wave. From the context of finishing, this is an ideal scenario when deformation induced removal of roughness features is of primary concern.

4.2.3. *Implications in a traditional finishing process — shot peening*

The aforementioned results can enable optimization of traditional finishing processes that rely on surface deformation. Towards this end, the geometry of indentation is analogous to that in shot peening which involves repeated impact of a component surface with hard media that is accelerated to a preset velocity range. Individual impacts result in plastic deformation of the surface which upon accumulation by repeated impact produces ultra-fine or nanocrystalline grains [3] and high compressive residual stresses [4]. In addition, mechanical interaction between the media and the surface results in evolution of its texture whose trajectory is determined by shot velocity and size [29]. Due to superior mechanical response of shot peened surfaces its utility as a finishing process for additively manufactured components is being explored [30]. Herein, similarity in process configuration makes insights obtained from indentation relatable to peening. For instance, observations in Fig. 8 indicate that process parameters must be tuned to concentrate deformation closer to the surface when harder microstructures are present near the surface. From the context of shot peening, this requirement can be met by using a combination of smaller shot diameter and smaller impact velocity. On the contrary, for finishing a surface featuring large roughness as shown in Fig. 9, larger shots are required in peening treatment. These contradicting factors suggest that there is an optimum shot size that can finish a rough surface that simultaneously features a microstructure gradient. Further, the numerical framework demonstrated in Fig. 7 can provide a starting point for optimizing this parameter. Formulation of a generic framework that can be used to optimize various finishing process for arbitrary geometries will be the focus of future efforts.

5. Conclusions

The investigation of the mechanics of indentation of IN718 created by AM has yielded a numerical framework for prediction of mechanics of surface deformation of various microstructure/texture/defect structure combinations. By utilizing this framework, the following conclusions could be drawn:

1. Mechanics of indentation in additively manufactured specimens is complicated by surface roughness, graded microstructure zones near the surface and porosity defects.
2. Harder microstructures near the surface result in dissipation of plastic strains to larger zones underneath the surface. This presents a less than ideal scenario when the primary concern is to create a smooth surface using deformation based material removal. Preliminary analyses indicates that mitigation of roughness features on graded microstructures can be achieved by concentrating the deformation resulting from the finishing process near the surface. Further, this can be done by tuning finish process parameters such as media size.
3. The framework also suggests that high aspect ratio roughness features can be mitigated more easily by use of larger finishing media that results in a more uniform deformation field.

Data availability

All data is available upon request from corresponding author.

Declaration of competing interest

The authors declare that they have no known competing financial interests or personal relationships that could have appeared to influence the work reported in this paper.

CRediT authorship contribution statement

Mustafa Rifat: Created the experimental plan, performed indentation experiments, characterized the strain fields, characterized microstructures, and analyzed the results, played significant role in writing the draft. **Edward C. DeMeter:** Performed analysis of results, provided scientific input. **Saurabh Basu:** Conceived of the idea, performed analysis of results and played significant role in writing the draft.

Acknowledgment

This material is based upon work supported by the National Science Foundation under Grant No. 1825686.Any opinions, findings, conclusions or recommendations expressed in this material are those of the authors and do not necessarily reflect the views of the National Science Foundation.

References

[1] S. Bagehorn, J. Wehr, H. Maier, Application of mechanical surface finishing processes for roughness reduction and fatigue improvement of additively manufactured ti-6al-4v parts, Int. J. Fatigue 102 (2017) 135–142, http://dx.doi.org/10.1016/j.ijfatigue.2017.05.008, URL http://www.sciencedirect.com/science/article/pii/S0142112317302153.

[2] Z. Wang, S. Basu, T.G. Murthy, C. Saldana, Gradient microstructure and texture in wedge-based severe plastic burnishing of copper, J. Mater. Res. 33 (8) (2018) 1046–1056, http://dx.doi.org/10.1557/jmr.2018.58.

[3] Z. Wang, M. Rifat, C. Saldana, S. Basu, Quantifying the spread in crystallographic textures due to transients in strain path in shot-peening, Materialia 2 (2018) 231–249, http://dx.doi.org/10.1016/j.mtla.2018.08.005, URL http://www.sciencedirect.com/science/article/pii/S2589152918300656.

[4] Y. Zhang, Z. Han, K. Wang, K. Lu, Friction and wear behaviors of nanocrystalline surface layer of pure copper, Wear 260 (9) (2006) 942–948, http://dx.doi.org/10.1016/j.wear.2005.06.010, URL http://www.sciencedirect.com/science/article/pii/S0043164805003947.

[5] F. Sun, E.V. der Giessen, L. Nicola, Plastic flattening of a sinusoidal metal surface: A discrete dislocation plasticity study, Wear 296 (1) (2012) 672–680, http://dx.doi.org/10.1016/j.wear.2012.08.007, URL http://www.sciencedirect.com/science/article/pii/S0043164812002840.

[6] E. Yasa, J. Deckers, J.P. Kruth, The investigation of the influence of laser remelting on density, surface quality and microstructure of selective laser melting parts, Rapid Prototyping J. 17 (5) (2011) 317–327.

[7] J.-P. Choi, G.-H. Shin, S. Yang, D.-Y. Yang, J.-S. Lee, M. Brochu, J.-H. Yu, Densification and microstructural investigation of inconel 718 parts fabricated by selective laser melting, Powder Technol. 310 (2017) 60–66, http://dx.doi.org/10.1016/j.powtec.2017.01.030, URL http://www.sciencedirect.com/science/article/pii/S0032591017300402.

[8] A. Antonysamy, J. Meyer, P. Prangnell, Effect of build geometry on the beta-grain structure and texture in additive manufacture of ti6al4v by selective electron beam melting, Mater. Charact. 84 (2013) 153–168, http://dx.doi.org/10.1016/j.matchar.2013.07.012, URL http://www.sciencedirect.com/science/article/pii/S1044580313002131.

[9] Z. Wang, T.A. Palmer, A.M. Beese, Effect of processing parameters on microstructure and tensile properties of austenitic stainless steel 304l made by directed energy deposition additive manufacturing, Acta Mater. 110 (2016) 226–235, http://dx.doi.org/10.1016/j.actamat.2016.03.019, URL http://www.sciencedirect.com/science/article/pii/S1359645416301744.

[10] V. Popovich, E. Borisov, A. Popovich, V. Sufiiarov, D. Masaylo, L. Alzina, Functionally graded inconel 718 processed by additive manufacturing: Crystallographic texture, anisotropy of microstructure and mechanical properties, Mater. Des. 114 (2017) 441–449, http://dx.doi.org/10.1016/j.matdes.2016.10.075, URL http://www.sciencedirect.com/science/article/pii/S026412751631382X.

[11] B.E. Carroll, T.A. Palmer, A.M. Beese, Anisotropic tensile behavior of ti–6al–4v components fabricated with directed energy deposition additive manufacturing, Acta Mater. 87 (2015) 309–320, http://dx.doi.org/10.1016/j.actamat.2014.12.054, URL http://www.sciencedirect.com/science/article/pii/S135964541400980X.

[12] T. Mukherjee, W. Zhang, T. DebRoy, An improved prediction of residual stresses and distortion in additive manufacturing, Comput. Mater. Sci. 126 (2017) 360–372, http://dx.doi.org/10.1016/j.commatsci.2016.10.003, URL http://www.sciencedirect.com/science/article/pii/S0927025616304980.

[13] H. Helmer, A. Bauereiß, R. Singer, C. Körner, Grain structure evolution in inconel 718 during selective electron beam melting, Mater. Sci. Eng. A 668 (2016) 180–187, http://dx.doi.org/10.1016/j.msea.2016.05.046, URL http://www.sciencedirect.com/science/article/pii/S0921509316305536.

[14] A. Townsend, N. Senin, L. Blunt, R. Leach, J. Taylor, Surface texture metrology for metal additive manufacturing: a review, Precis. Eng. 46 (2016) 34–47, http://dx.doi.org/10.1016/j.precisioneng.2016.06.001, URL http://www.sciencedirect.com/science/article/pii/S0141635916300721.

[15] K. Tan, S. Yeo, Surface finishing on in625 additively manufactured surfaces by combined ultrasonic cavitation and abrasion, Addit. Manuf. 31 (2020) 100938, http://dx.doi.org/10.1016/j.addma.2019.100938, URL http://www.sciencedirect.com/science/article/pii/S2214860419308383.

[16] W. Grzesik, P. Niesłony, P. Laskowski, Determination of material constitutive laws for inconel 718 superalloy under different strain rates and working temperatures, J. Mater. Eng. Perform. 26 (12) (2017) 5705–5714, http://dx.doi.org/10.1007/s11665-017-3017-8.

[17] S. Abolghasem, S. Basu, M.R. Shankar, Quantifying the progression of dynamic recrystallization in severe shear deformation at high strain rates, J. Mater. Res. 28 (15) (2013) 2056–2069, http://dx.doi.org/10.1557/jmr.2013.201.

[18] F.J. Humphreys, M. Hatherly, Recrystallization and Related Annealing Phenomena, Elsevier, 2012.

[19] A. Acharya, R.J. Knops, An observation on the experimental measurement of dislocation density, J. Elasticity 114 (2) (2014) 275–279, http://dx.doi.org/10.1007/s10659-013-9437-2.

[20] A. Beaudoin, A. Acharya, S. Chen, D. Korzekwa, M. Stout, Consideration of grain-size effect and kinetics in the plastic deformation of metal polycrystals, Acta Mater. 48 (13) (2000) 3409–3423, http://dx.doi.org/10.1016/S1359-6454(00)00136-1, URL http://www.sciencedirect.com/science/article/pii/S1359645400001361.

[21] T. Narutani, J. Takamura, Grain-size strengthening in terms of dislocation density measured by resistivity, Acta Metall. Mater. 39 (8) (1991) 2037–2049, http://dx.doi.org/10.1016/0956-7151(91)90173-X, URL http://www.sciencedirect.com/science/article/pii/095671519190173X.

[22] F. Yuan, P. Jiang, J. Xie, X. Wu, Analysis of spherical indentation of materials with plastically graded surface layer, Int. J. Solids Struct. 49 (3) (2012) 527–536, http://dx.doi.org/10.1016/j.ijsolstr.2011.10.018, URL http://www.sciencedirect.com/science/article/pii/S0020768311003568.

[23] I. Choi, A. Detor, R. Schwaiger, M. Dao, C. Schuh, S. Suresh, Mechanics of indentation of plastically graded materials—ii: Experiments on nanocrystalline alloys with grain size gradients, in: Bridging Scales in Mechanics - where are the Bottom and the Top? the Needleman-Tvergaard Solid Mechanics Symposium, J. Mech. Phys. Solids 56 (1) (2008) 172–183, http://dx.doi.org/10.1016/j.jmps.2007.07.006, URL http://www.sciencedirect.com/science/article/pii/S002250960700155X.

[24] A.A. Thompson, Yielding in nickel as a function of grain or cell size, Acta Metall. 23 (11) (1975) 1337–1342, http://dx.doi.org/10.1016/0001-6160(75)90142-X, URL http://www.sciencedirect.com/science/article/pii/000161607590142X.

[25] C. Zhang, F. Chen, Z. Huang, M. Jia, G. Chen, Y. Ye, Y. Lin, W. Liu, B. Chen, Q. Shen, L. Zhang, E.J. Lavernia, Additive manufacturing of functionally graded materials: A review, Mater. Sci. Eng. A 764 (2019) 138209, http://dx.doi.org/10.1016/j.msea.2019.138209, URL http://www.sciencedirect.com/science/article/pii/S0921509319309955.

[26] D. Meyer, N. Wielki, Internal reinforced domains by intermediate deep rolling in additive manufacturing, CIRP Ann. 68 (1) (2019) 579–582, http://dx.doi.org/10.1016/j.cirp.2019.04.012, URL http://www.sciencedirect.com/science/article/pii/S0007850619300381.

[27] R.R. Dehoff, M.M. Kirka, W.J. Sames, H. Bilheux, A.S. Tremsin, L.E. Lowe, S.S. Babu, Site specific control of crystallographic grain orientation through electron beam additive manufacturing, Mater. Sci. Technol. 31 (8) (2015) 931–938, http://dx.doi.org/10.1179/1743284714Y.0000000734.

[28] S. Hassani-Gangaraj, A. Moridi, M. Guagliano, A. Ghidini, M. Boniardi, The effect of nitriding, severe shot peening and their combination on the fatigue behavior and micro-structure of a low-alloy steel, in: 9th Fatigue Damage of Structural Materials Conference, Int. J. Fatigue 62 (2014) 67–76, http://dx.doi.org/10.1016/j.ijfatigue.2013.04.017, URL http://www.sciencedirect.com/science/article/pii/S0142112313001230.

[29] E. Nordin, B. Alfredsson, Measuring shot peening media velocity by indent size comparison, J. Mater Process. Technol. 235 (2016) 143–148, http://dx.doi.org/10.1016/j.jmatprotec.2016.04.012, URL http://www.sciencedirect.com/science/article/pii/S0924013616301029.

[30] A.H. Maamoun, M.A. Elbestawi, S.C. Veldhuis, Influence of shot peening on alsi10mg parts fabricated by additive manufacturing, J. Manuf. Mater. Process. 2 (3) (2018) 40.